Journal of Advanced Ceramics
2023, **12**(7): 1331–1344
https://doi.org/10.26599/JAC.2023.9220754
ISSN 2226-4108
CN 10-1154/TQ

Research Article

Enhanced piezoelectricity in Na and Ce co-doped $CaBi_4Ti_4O_{15}$ ceramics for high-temperature applications

Zimeng Hu[a], Vladimir Koval[b], Hangfeng Zhang[a], Kan Chen[a], Yajun Yue[c,d], Dou Zhang[e,*], Haixue Yan[a,*]

[a]*School of Engineering and Materials Science, Queen Mary University of London, London E1 4NS, UK*
[b]*Institute of Materials Research, Slovak Academy of Sciences, Kosice 04001, Slovakia*
[c]*Spallation Neutron Source Science Center, Dongguan 523803, China*
[d]*Institute of High Energy Physics, Chinese Academy of Sciences (CAS), Beijing 100049, China*
[e]*State Key Laboratory of Powder Metallurgy, Central South University, Changsha 410083, China*

Received: December 25, 2022; Revised: April 15, 2023; Accepted: April 16, 2023

Abstract: The sodium (Na) and Ce co-doped calcium bismuth titanate (CBT; $CaBi_4Ti_4O_{15}$) Aurivillius ceramics in a $Ca_{1-x}(Na_{0.5}Ce_{0.5})_xBi_4Ti_4O_{15}$ (CNCBT; doping content (x) = 0, 0.03, 0.05, 0.08 and 0.12) system were synthesized by the conventional solid-state sintering method. All compositions show a single-phase orthorhombic (space group: $A2_1am$) structure at room temperature. The shift of the Curie point (T_C) towards lower temperatures (T) on doping results from the increased tolerance factor (t). The substitution-enhanced ferroelectric performance with large maximum polarization (P_m) and facilitated domain switching is evidenced by the developed electrical polarization–electric field (P–E) and electrical current–electric field (I–E) hysteresis loops. The piezoelectric coefficient (d_{33} = 20.5± 0.1 pC/N) of the x = 0.12 sample is about four times larger than that of pure CBT. The improved piezoelectric properties can be attributed to the high remanent polarization (P_r) and relatively high dielectric permittivity (ε'). In addition, multi-sized (micron and sub-micron) domain structures were observed in the CNCBT ceramics by the piezoresponse force microscope (PFM). The multiple-sized ferroelectric domain structure with smaller domains is beneficial to the easy domain switching, enhanced ferroelectric performance, and improved piezoelectric properties of the CNCBT ceramics. The designed Aurivillius-phase ferroelectric ceramics with the T_C around 765 ℃ and high piezoelectric coefficient (d_{33}) are suitable for high-temperature piezoelectric applications.

Keywords: Aurivillius-phase ceramics; high Curie point; domain switching; piezoelectric properties

* Corresponding authors.
E-mail: D. Zhang, dzhang@csu.edu.cn;
H. Yan, h.x.yan@qmul.ac.uk

1 Introduction

Bismuth layer-structured ferroelectrics (BLSFs) belong to a family of Aurivillius-phase materials characterized by a general formula of $(Bi_2O_2)^{2+}(A_{m-1}B_mO_{3m+1})^{2-}$ (where A is a divalent ion or a combination of alkali and lanthanides occupying the dodecahedral coordination site, B is usually a transition metal ion occupying the octahedral coordination site, and m is the number of BO_6 octahedra in the $(A_{m-1}B_mO_{3m+1})^{2-}$ perovskite layer separated by two $(Bi_2O_2)^{2+}$ layers [1]). The m can be an integer number or a rational number (1.5, 2, 2.5, 3, etc.) typically not bigger than 5 to ensure good dielectric, ferroelectric, and piezoelectric properties of BLSFs. Calcium bismuth titanate (CBT; $CaBi_4Ti_4O_{15}$), as a member of the m = 4 family of BLSFs, is a potential candidate for high-temperature piezoelectric and ferroelectric applications such as sensors, filters, or oscillators because of its high Curie point ($T_C \approx 790$ ℃), good thermal stability, low aging, and low dielectric loss tangent (tanδ) [2,3]. However, a commercial application of CBT ceramics is limited due to their weak piezoelectricity (piezoelectric coefficient (d_{33}) < 5 pC/N). The relatively low values of d_{33} are related to a high coercive field (E_c) of CBT, which makes it difficult to switch ferroelectric domains by direct current (DC) or alternating current (AC) poling.

Numerous experimental techniques and methods have been developed to improve the piezoelectric properties of CBT. It was demonstrated that the spark plasma sintering [4], cold-pressing [5], and ion engineering methods [6–8] can effectively improve the piezoelectric and ferroelectric performances of BLSFs. Among these approaches, ion doping appears to be the most viable method for industrial fabrication as it enables to easily modify the sintering activity, microstructure, and electrical properties at low costs. It has been reported that a partial substitution of CBT at A sites with lanthanides, e.g., La, can greatly improve its piezoelectric properties [8]. The d_{33} of La-doped CBT was about 11 pC/N, and the high piezoelectricity was explained by the increased Bi : Ca ratio [8]. However, the T_C decreases on La doping, which hinders the use of this material at high temperatures (T). An enhancement of the d_{33} (~15 pC/N) and a small shift of T_C towards higher temperatures were observed in vanadium (V)-doped CBT ceramics [9]. The V-doping effects were explained by the higher valence of V^{5+} ions, if compared to the valence of Ti^{4+} ions, introducing the cation vacancy, which may improve the structure distortion, and thus increase T_C [9,10]. Aside from the single doping, equally co-doped CBT ceramics at the A site with lanthanides (e.g., Er^{3+}, Nd^{3+}, Ho^{3+}, and Ce^{3+}) and alkaline metals (e.g., Na^+, Li^+, and K^+) have been recently proposed for the investigation of improved ferroelectric and piezoelectric properties [11–15]. In Ref. [12], it has been found that $Ca_{1-x}(A,Ce)_{x/2}Bi_4Ti_4O_{15}$ (x is the doping content, and A = Li, Na, and K) ceramics exhibit high electrical resistivity and d_{33} at high temperatures compared to pure $CaBi_4Ti_4O_{15}$ ceramics. However, neither the ferroelectric behaviour nor the domain morphology of the doped ceramics was investigated thoroughly. A comprehensive understanding of the effect of the double doping with alkaline and rare-earth ions on the crystal structure, domain structure, dielectric, piezoelectric, and ferroelectric properties of CBT is still missing.

In the present study, Na was chosen for co-doping of the above $Ca_{1-x}(A,Ce)_{x/2}Bi_4Ti_4O_{15}$ system, because Li^+ is known easily evaporated during sintering at high temperatures, and K^+ can dramatically lower the T_C due to its large radius [12]. The designed $Ca_{1-x}(Na_{0.5}Ce_{0.5})_xBi_4Ti_4O_{15}$ (CNCBT; x = 0, 0.03, 0.05, 0.08, and 0.12) ceramic system is investigated for the underlying mechanisms between crystal structures, domain morphologies, and electrical properties. Moreover, the domain engineering approach is adapted in the preparation of the Na and Ce co-doped samples to obtain a multiple domain structure with a reduced E_c, large maximum polarization (P_m), and relatively high dielectric permittivity (ε'). The lower E_c and larger ε' are crucial to enhancing the d_{33} as well as the electromechanical coupling factors in Aurivillius CBT-based ceramics. Thus, the proposed approach provides a guide for future material design and performance optimization of Aurivillius-phase ceramics in high-temperature piezoelectric sensors and actuators.

2 Materials and methods

The $Ca_{1-x}(Na_{0.5}Ce_{0.5})_xBi_4Ti_4O_{15}$ ceramics with x = 0, 0.03, 0.05, 0.08, and 0.12 (abbreviated hereafter as CBT, CNCBT3, CNCBT5, CNCBT8, and CNCBT12, respectively) were synthesized via the traditional solid-state reaction method. The starting materials were powders of $CaCO_3$ (Alfa Aesar, purity > 99.8%),

$NaCO_3$ (Alfa Aesar, purity = 99.8%), CeO_2 (Sigma Aldrich, purity = 99.9%), TiO_2 (Sigma Aldrich, purity = 99.8%), and Bi_2O_3 (Sigma Aldrich, purity = 99.9%). After pre-heating at 200 ℃ for 24 h, these chemicals were weighed according to the stoichiometric composition. The mixture was ground in ethanol for 6 h with Y-stabilized ZrO_2 balls in nylon bottles using a planetary ball mill (Planetary Mill PULVERISETTE 5/4, FRITSCH, German). The slurry was dried at 100 ℃ overnight. The dried powders were calcined at 800 ℃, and then at 900 ℃ for 2 h in a programmable furnace (30-3000 C, Nabertherm, UK). The calcined powders were ball-milled again for 6 h to reduce the particle size. Then, 5 wt% polyvinyl alcohol (PVA) was added into the calcined powders, and the mixture was pressed into disks (13 mm in diameter and 1–2 mm in thickness) at a pressure of 100 MPa. The pellets were heated at 800 ℃ for 2 h without the lid to remove the PVA binder. After that, the pellets were inserted into an alumina crucible, covered by the coarse ZrO_2 powders and sintered at 1150 ℃ for 2 h in the air.

The crystal structures of the sintered CBT-derived ceramics were investigated on crushed powders over the 2θ range from 5° to 120° using an X-ray diffractometer (Cubix, PANalytical, the Netherlands) with Ni-filtered Cu Kα radiation (λ = 1.5418 Å). The Rietveld refinement analysis of the X-ray diffraction (XRD) data within a wide range was performed by means of the General Structure Analysis System (GSAS) software [16] combined with the EXPGUI interface [17]. The microstructures of the thermally etched ceramics (the well-polished ceramics were annealed at a temperature typically 100 ℃ below the sintering temperature for 2 h) [18,19] were observed using a scanning electron microscope (SEM; FEI Inspect-F, USA). The grains are plate-like with similar thicknesses. The average grain size (perpendicular to the thickness direction) is derived from the average grain length within the scanning area, which was measured and calculated via the Image J software. The ferroelectric domain structure was studied on the unpoled samples after well mirror polishing without annealing by the piezoresponse force microscope (PFM, Bruker, USA) both in the vertical and lateral modes. The scanning area is 5 μm × 5 μm, and the drive amplitude of the electric field (E) is 10 V. The surface element analysis of ceramics was performed with an X-ray photoelectron spectrometer (Nexsa XPS system, Thermo Fisher Scientific, USA). The X-ray photoelectron spectroscopy (XPS) spectra were fitted by the Gaussian–Lorentzian product function implemented in the commercial Avantage software [20]. For the dielectric, ferroelectric, and piezoelectric measurements, the as-sintered ceramics were electroded on major surfaces by a platinum paste (C2011004D5, Gwent Electronic Materials Ltd., UK). The temperature dependence of the relative ε' and tanδ was measured in the temperature range of 25–900 ℃ with a heating rate of 3 ℃/min at various frequencies from 1 kHz to 1 MHz with an LCR meter (4284A, Agilent, USA) connected to a tube furnace. Both the electrical polarization–electric field (P–E) and electrical current–electric field (I–E) loops were measured in silicon oil at room temperature (RT) using a ferroelectric tester (NPL made with a pair of NXB2-AL nanosensors, HP33120A function generator and LabView software controlled, Teddington, UK) [21]. The testing frequency of the triangular voltage waveforms was set to 10 Hz. The samples were poled in silicone oil under a DC field of 8 kV/mm at 150 ℃ for 10–15 min, and then depoled at selected temperatures for 2 h from RT to 700 ℃. The d_{33} was measured with a d_{33} meter (ZJ-3AN, Institute of Acoustics Academia, Beijing, China). The planar and thickness electromechanical coupling factors (K_p and K_t) and the mechanical coupling factor (Q_m) were determined by the resonance–antiresonance method [22,23] using the data collected by an LCR meter (4284A, Agilent, USA).

3 Results and discussion

The measured relative densities are 96.1%, 96.1%, 96.2%, 96.2%, and 96.1% for $Ca_{1-x}(Na_{0.5}Ce_{0.5})_xBi_4Ti_4O_{15}$ (x = 0, 0.03, 0.05, 0.08, and 0.12) ceramics, respectively. Figure S1 in the Electronic Supplementary Material (ESM) shows the XRD patterns of the $Ca_{1-x}(Na_{0.5}Ce_{0.5})_xBi_4Ti_4O_{15}$ (x = 0, 0.03, 0.05, 0.08 and 0.12) ceramics at RT. The labelled hkl indices correspond to those of the reference orthorhombic-structured CBT samples with the $A2_1am$ symmetry (PDF#52-1640). The Na and Ce co-doped CBT ceramics show almost the same diffraction reflections as pure CBT without any traces of a secondary phase. Hence, the Na and Ce ions are assumed to enter the lattice and form the m = 4 Aurivillius phase at RT. The Rietveld structure refinements of the XRD data were

carried out to further investigate the structural changes induced by the Na and Ce doping (Fig. 1). The refinement details as well as the refined structure parameters are given in Table S1 in the ESM. The lattice expansion, as shown in Fig. 1(f), can be probably attributed to the bigger average ionic radii of Na^{+} (1.39 Å) and Ce^{3+} (1.34 Å) ions, if compared to that of Ca^{2+} (1.34 Å) [24]. Few Ce^{4+} ions (less than half of Ce^{3+} ions) with a smaller radius (1.14 Å) also existed here supporting by the later XPS analysis, which is not the dominant reason for the volume change.

The microstructure images of the CNCBT ceramics are shown in Fig. 2. Dense CNCBT ceramic samples were obtained by the optimized sintering process, confirming the calculated density of the sintered samples by the Archimedes method. The observation of anisotropic plate-like shaped grains is in accordance with the data previously reported on single-phase Aurivillius ceramics [15]. The average grain sizes decrease slightly on doping from 2.85±1.13 μm (CBT) to 2.68±1.08 μm (CNCBT3), 2.55±1.05 μm (CNCBT5), 2.15±0.85 μm (CNCBT8), and 1.96± 0.75 μm (CNCBT12) (Fig. 2(f)), which can be possibly explained by the co-doping of Na and Ce ions with different radii compared with Ca^{2+}. Co-dopants with

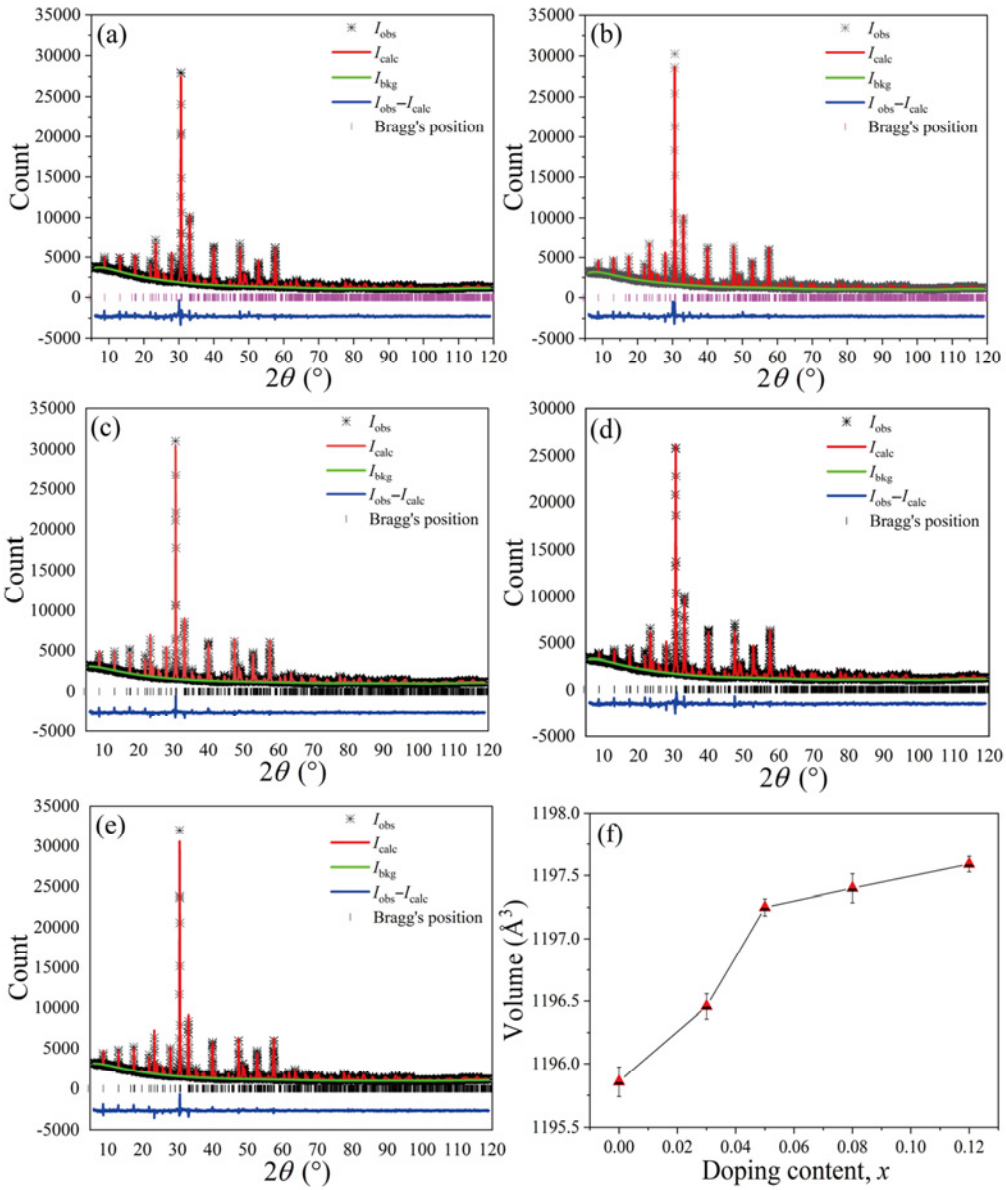

Fig. 1 Rietveld refinements of the XRD patterns for (a) CBT, (b) CNCBT3, (c) CNCBT5, (d) CNCBT8, and (e) CNCBT12 ceramics. (f) Compositional dependence of unit cell volume (I_{obs}: measured pattern, I_{calc}: calculated pattern, and I_{obs}–I_{calc}: difference).

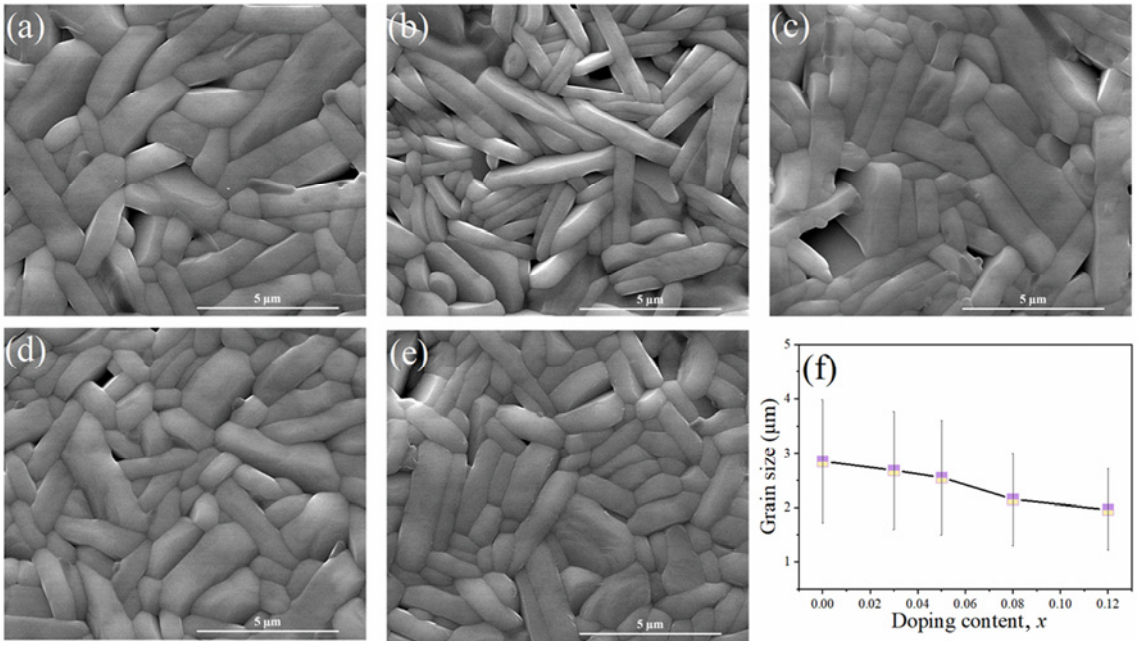

Fig. 2 Micrographs of (a) CBT, (b) CNCBT3, (c) CNCBT5, (d) CNCBT8, and (e) CNCBT12 ceramics (after thermal etching).(f) Compositional dependence of grain size.

different radii can produce the local stress field at the lattice level, which is the barrier for the diffusion of ions. Hence, the grain size decreases with the increasing x, which can be attributed to the lower diffusivity caused by the local stress field [25].

To explore the chemical states of oxygen and check for an existence of oxygen vacancies (O_{vac}), the surface elemental analysis on CNCBT ceramics was carried out by the XPS. The fitted O 1s XPS spectra are shown in Fig. 3. The deconvolution of the O 1s spectral peak

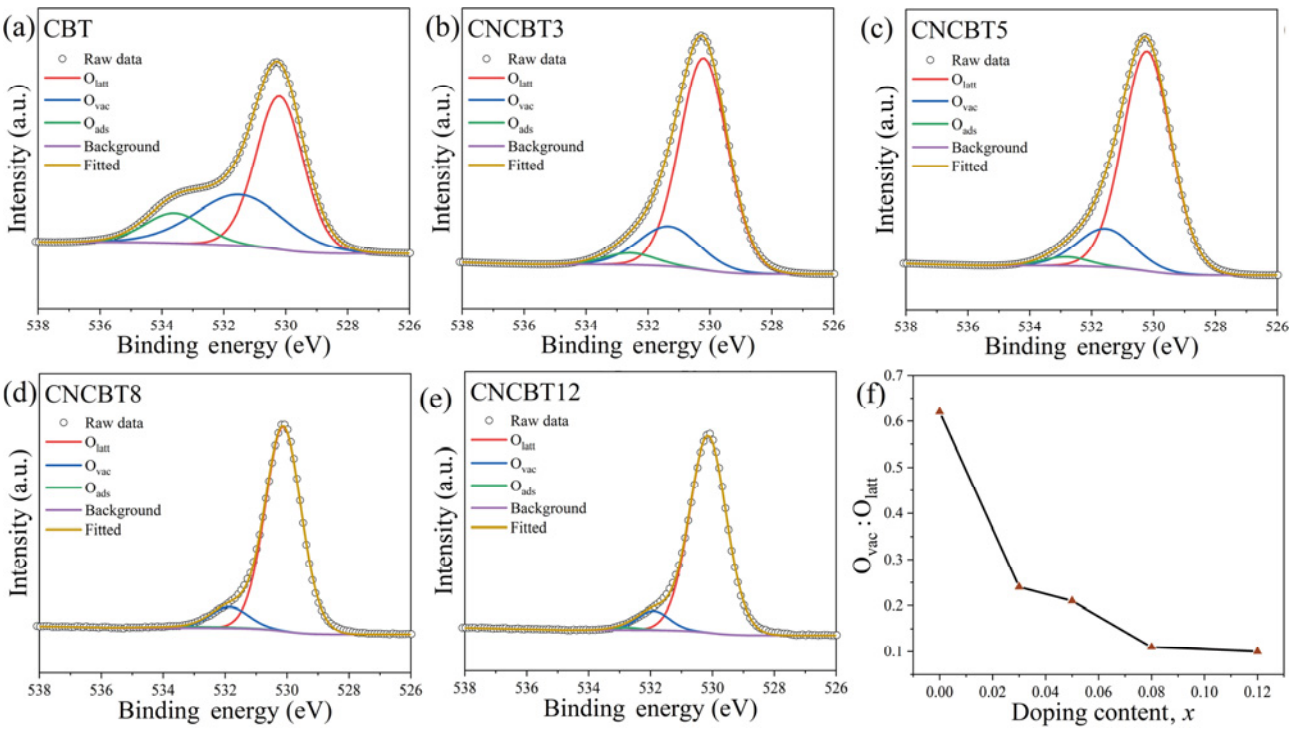

Fig. 3 Fitted XPS spectra of O 1s peaks for (a) CBT, (b) CNCBT3, (c) CNCBT5, (d) CNCBT8, and (e) CNCBT12 ceramics. (f) Compositional dependence of O_{vac} : O_{latt} ratio.

gives three overlapping peaks—The first peak lattice oxygen (O_{latt}) at a lower binding energy (~530 eV) is associated with the intrinsic state of O (the red line), the second peak O_{vac} at a moderate binding energy (~531 eV) corresponds to the oxygen in the deficient region (the blue line), and the third peak of the adsorbed oxygen (O_{ads}) at a higher binding energy (~533 eV) can be linked with O_{ads} from the air (the green line) [26,27]. The ratio of O_{vac} : O_{latt} corresponds to the concentration of oxygen vacancies in the prepared compositions [28]. The binding energies for three peaks and the O_{vac}: O_{latt} ratio are listed in Table S2 in the ESM. The estimated O_{vac} : O_{latt} values decrease from 0.62 to 0.24, 0.21, 0.12, and 0.10 for the samples of CBT, CNCBT3, CNCBT5, CNCBT8, and CNCBT12, respectively.

The existence of oxygen vacancies can be possibly due to the reduction of Ti^{4+} cations during the sintering, which is common in piezoelectric ceramics prepared by the solid-state sintering method. The underlying mechanism can be described by the Kröger–Vink notation, as reported in other perovskite ferroelectric ceramics [29].

$$2Ti_{Ti}^{\times} + O_O^{\times} \rightarrow 2Ti_{Ti}' + V_{\ddot{O}} + \frac{1}{2}O_2 \quad (1)$$

The holes were then generated because samples adsorb ambient oxygen on the specimen surface during cooling based on Reaction (2):

$$\frac{1}{2}O_2 + V_{\ddot{O}} \rightarrow O_O^{\times} \rightarrow 2h^{\bullet} \quad (2)$$

The fitted Ti 2p XPS spectra including six well de-convoluted peaks, as presented in Fig. S2 in the ESM, clearly demonstrate the existence of Ti^{3+} and Ti^{4+} for all CNCBT ceramics [29,30]. All binding energies and Ti^{3+} : Ti^{4+} ratios deduced from Fig. S2 are listed in Table S3 in the ESM. The decreasing trend of Ti^{3+} : Ti^{4+} is consistent with that of the oxygen vacancies. In addition, the high-resolution Ce XPS spectra well fitted by eight typical peaks support the co-existence of Ce^{3+} and Ce^{4+} cations [31], as presented in Fig. S3 in the ESM. All binding energies and semi-quantified Ce^{3+} : Ce^{4+} ratios deduced from Fig. S3 in the ESM are listed in Table S4 in the ESM. The Ce as the donor dopant can provide extra electrons to reduce the concentration of holes, which can be expressed by Reactions (3)–(5) [32]:

$$Ce^{4+} \xrightarrow{Ca^{2+}} Ce_{Ca}^{\cdot} + 2e' \quad (3)$$

$$Ce^{3+} \xrightarrow{Ca^{2+}} Ce_{Ca}^{\cdot} + e' \quad (4)$$

$$\frac{1}{2}O_2 + V_{\ddot{O}} + 2e' \rightarrow O_O^{\times} \quad (5)$$

Figure 4 displays the plots of ε' and $\tan\delta$ as a function of T for the CNCBT ceramics. All compositions show a sharp $\varepsilon'(T)$ peak near 800 ℃, indicating a narrow ferroelectric to paraelectric phase transition. The T_C for CBT, CNCBT3, CNCBT5, CNCBT8, and CNCBT12 are 784±1, 783±1, 781±1, 770±1, and 765±1 ℃, respectively (at 500 kHz). These values match well with the previously reported Aurivillius materials [33]. The substitution-induced decrease of T_C can be ascribed to the changes of tolerance factor (t).

$$t = (R_A + R_O)/[\sqrt{2}(R_B + R_O)] \quad (6)$$

where R_A, R_O, and R_B are the effective average radii of divalent ions, oxygen, and ions at the octahedral sites, respectively. In general, T_C decreases when t increases due to the structure distortion [10]. Upon Na^+ and $Ce^{3+/4+}$ co-doping, the t increases from 0.9730 to 0.9733, 0.9735, 0.9739, and 0.9742 for CBT, CNCBT3, CNCBT5, CNCBT8, and CNCBT12 ceramics, respectively, which is consistent with the reduction of T_C.

With the increasing amount of Na and Ce ions, the frequency dependence of permittivity especially at high frequencies is weakened. Specifically, the enhanced dielectric dispersion (ε'_m(100 kHz) − ε'_m(1 kHz)) decreases from 595 to 415, 280, 185, and 160 for the CBT, CNCBT3, CNCBT5, CNCBT8, and CNCBT12 ceramics, respectively, which can be attributed to the reduction of oxygen vacancies. Above T_C, the permittivity drops greatly, but then it increases again due to the space-charge effects activated by the thermal energy, as reported for BNT-based dielectrics [34]. For temperatures between T_C and 810 ℃, the Curie–Weiss (C–W) behaviour of the permittivity was investigated by Eq. (7) [35]:

$$\frac{1}{\varepsilon'} = \frac{T - T_0}{C} \quad (7)$$

Figure 4(f) shows plots of T_0, T_C, and C (obtained from the C–W fits at 500 kHz) of the CNCBT ceramics against x. The difference between T_0 and T_C indicates the first-order phase transition in all samples. Both T_0 and T_C decrease with the substitution-driven increase of the t, as discussed above. The calculated C is in the magnitude of 10^4 for all the compositions and matches well with the value reported for other dielectrics with a perovskite structure [36].

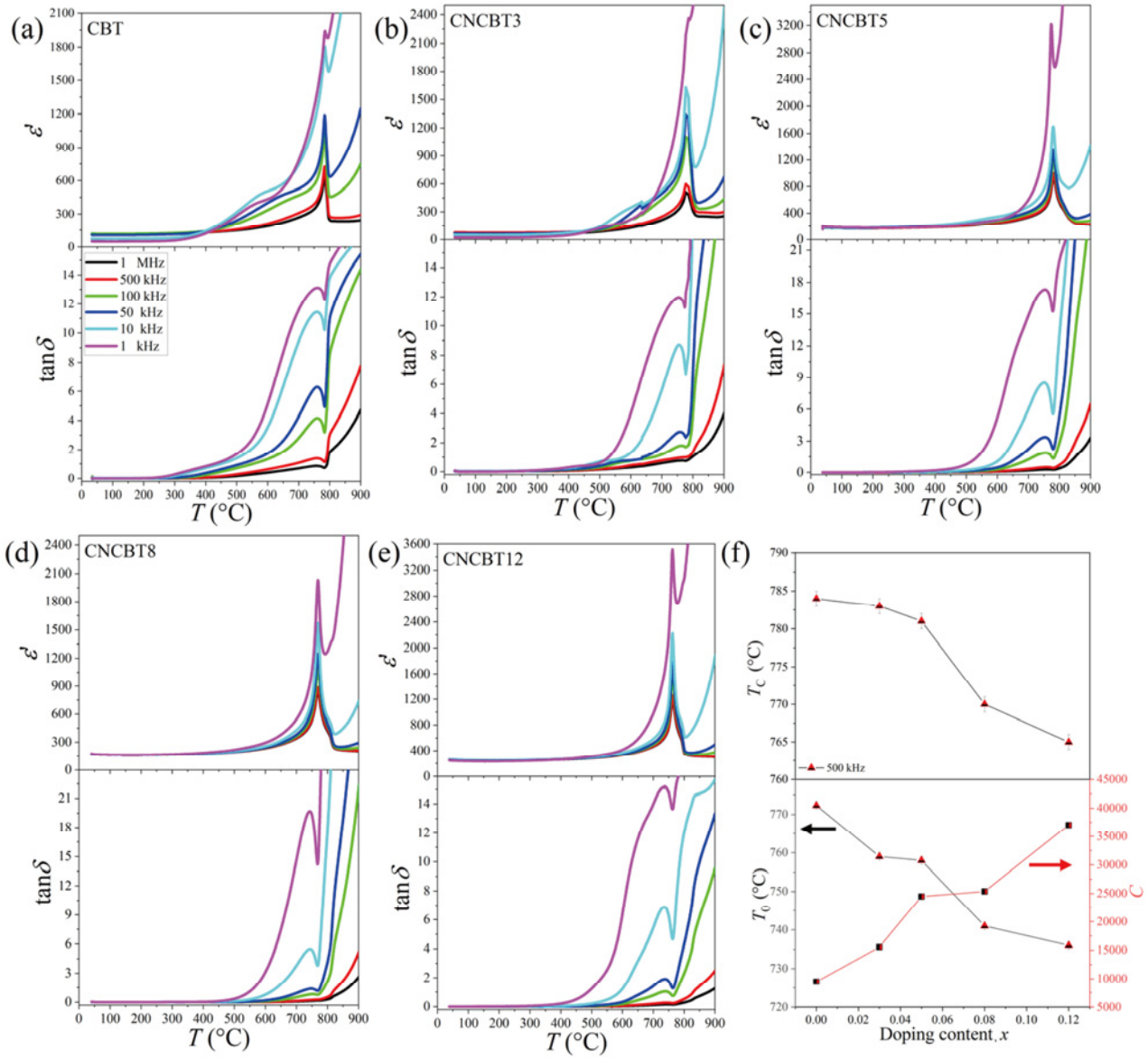

Fig. 4 Temperature dependence of ε' and tanδ at six selected frequencies for (a) CBT, (b) CNCBT3, (c) CNCBT5, (d) CNCBT8, and (e) CNCBT12 ceramics. (f) T_C, C–W temperature (T_0), and C–W constant (C) against x.

The loss is related to the AC conductivity and frequency-independent DC conductivity [37]. In Fig. 4, high losses at low frequencies can be attributed to contributions both from the friction of dipoles and DC conductivity. At high frequencies, the contribution of the friction of dipoles is dramatically decreased because many dipoles cannot follow the applied AC field, which indicates that the loss measured at high frequencies is dominated by DC conductivity. In Fig. 4, the loss measured at 1 MHz below 500 ℃ decreases with the increasing x, which suggests that the developed ceramics show high resistivity below 500 ℃. Obviously, the tanδ exhibit a peak below T_C (at about 750 ℃) due to the enhanced viscous movement of ferroelectric domain walls near the T_C. Additionally, an anomaly (a small broad peak) is observed in CBT and CNCBT3 around 600 ℃ and can be attributed to the thermally activated oxygen ion jump mechanism proposed in Ref. [38].

The representative topography and out-of-plane (OOP) and in-plane (IP) PFM amplitude and phase images of the $Ca_{1-x}(Na_{0.5}Ce_{0.5})_xBi_4Ti_4O_{15}$ (x = 0, 0.05 and 0.12) ceramics within a selected area of 5 μm × 5 μm are shown in Figs. 5(a)–5(c). The complex ferroelectric domain structure with micron/sub-micron sized domains and different polarization orientations is evidenced by

the distinguishable phase contrast between the bright areas or dots and the brown regions [39]. The roughness for scanned ceramics is pretty low (within 20 nm) though some scratches can be seen in the topography images, which do not affect the amplitude and phase images greatly because scratches are not overlapped with domain walls. It is obvious that the piezoelectric response in the lateral plane is higher than that of the vertical PFM images supported by the absolute piezoresponse in the amplitude images and the large phase contrast in the phase images, which can be explained by the polarization vector for CNCBT ceramics along the *a*-axis, i.e., perpendicular to the thickness plane of plate-like grains [40]. Usually, grains of Aurivillius phase ceramics with an even number of *m* prefer thickness-plane oriented, which do not contribute to a vertical PFM response because there is no polarization along *c*-axis according to their space group $A2_1am$, as shown by the domains indicated by the red circles. However, some domains (indicated by the blue circles in the PFM phase images) show high response in the vertical mode and weak response in the lateral mode, suggesting that lateral-plane oriented grains exist in the non-textured ceramics. Overall, both thickness-plane oriented and lateral-plane oriented grains exist in the prepared CNCBT ceramics. Strip-like domains, as denoted by the white arrows in Figs. 5(a) and 5(b), represent non-180° domains, which are 90° domain walls in orthorhombic-structured piezoelectric ceramics [41,42]. Moreover, smaller domains with nanometer sizes were observed in highly doped CNCBT ceramics like CNCBT12, and the average domain sizes are 0.28, 0.25, and 0.23 μm for CBT, CNCBT5, and CNCBT12 samples, respectively, calculated from the PFM line profile analysis [43], as shown in Figs. 5(d)–5(f). As shown in Fig. 2(f), the

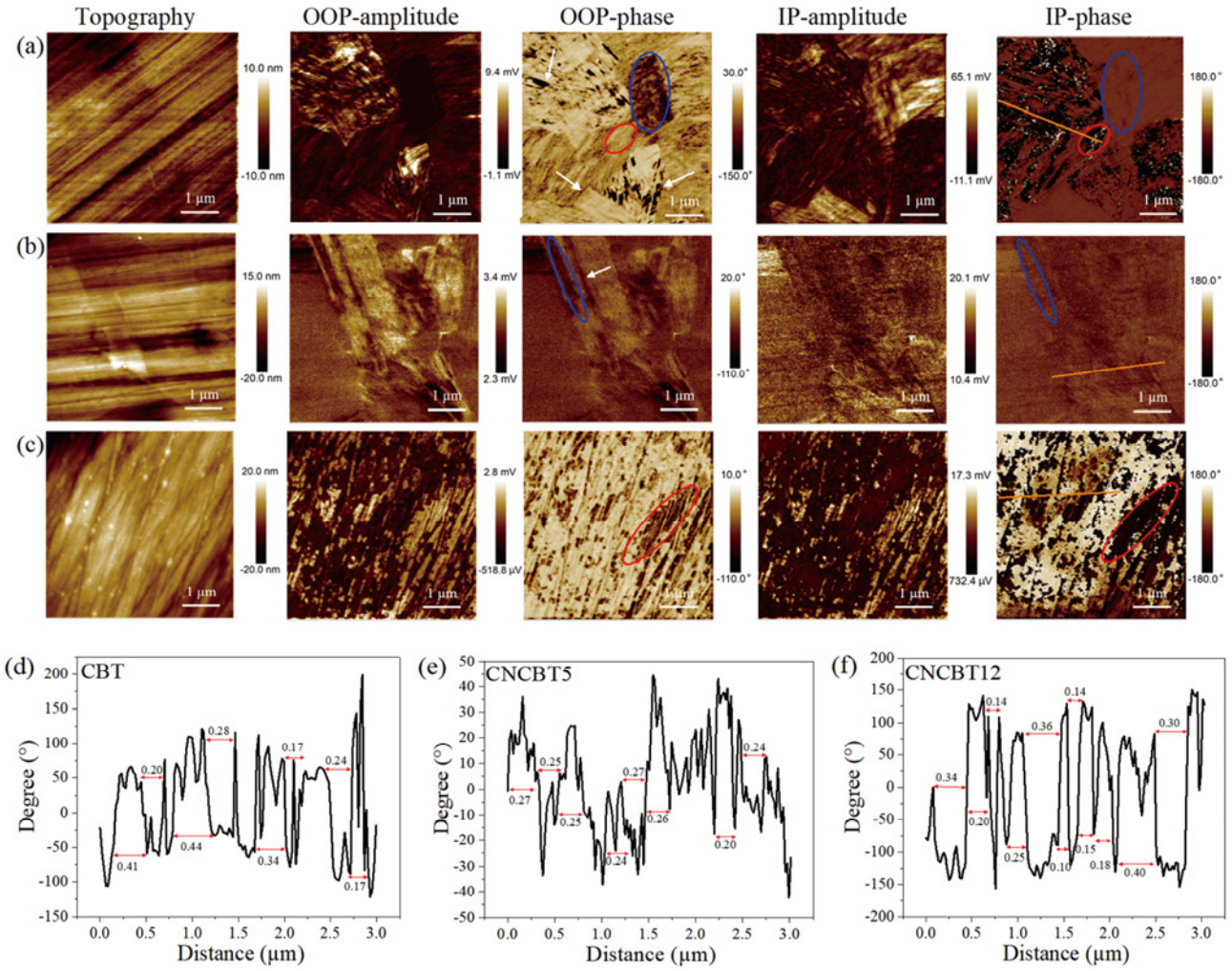

Fig. 5 (a–c) Topography and OOP and IP PFM amplitude and phase images of polished $Ca_{1-x}(Na_{0.5}Ce_{0.5})_xBi_4Ti_4O_{15}$ (x = 0, 0.05, and 0.12) ceramics. (d–f) Corresponding line profile analyses deduced from the orange lines in the IP phase images.

grain size decreases with the increasing x. In this case, small domains are favoured in highly doped CNCBT ceramics with a high grain boundary density due to the small grain size in order to minimize the strain energy caused by grain boundaries [44,45]. It is assumed that smaller ferroelectric domains are responsible for the increased dielectric permittivity and ferroelectric remanent polarization (P_r) and d_{33} [46,47].

The *P*–*E* and *I*–*E* hysteresis loops for the CNCBT ceramics measured at RT are presented in Fig. 6. While the current peaks corresponding to the domain switching are observed in the *I*–*E* loops (marked by the blue arrows) for the Na and Ce co-doped ceramics, pure CBT does not exhibit the ferroelectric switching up to a maximum E of 150 kV/cm. It is worth mentioning that the E of the current peak in *I*–*E* loops does not exactly match with the field where the slope of polarization is the largest in *P*–*E* loops. This inconsistency in the fields can be attributed to the presence of charged defects (e.g., oxygen vacancies) in

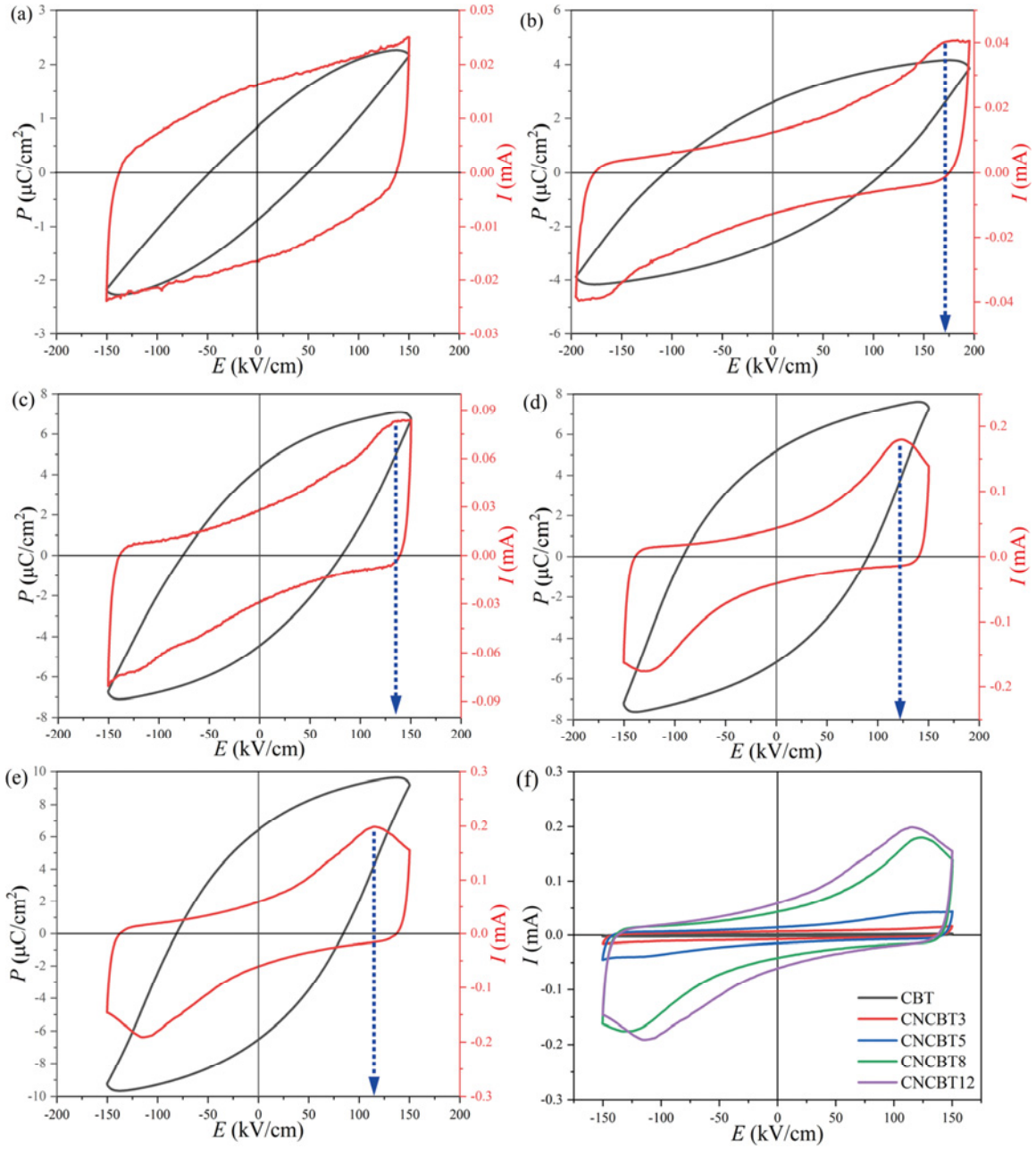

Fig. 6 *P*–*E* and *I*–*E* hysteresis loops for (a) CBT, (b) CNCBT3, (c) CNCBT5, (d) CNCBT8, and (e) CNCBT12 ceramics, as recorded at RT (the current peaks are indicated by the blue arrows). (f) *I*–*E* hysteresis loops for all CNCBT ceramics measured at 150 kV/cm and RT.

the ceramics [48,49]. Generally, in Aurivillius-phase ferroelectric ceramics, a high E needs to be applied to switch ferroelectric domains pinned by oxygen vacancies, which often causes dielectric breakdown of ceramics. For the CBT samples, the highest current at the maximum E is contributed by electrical conductivity. The E_c, at which the switching process occurs, decreases from 165 kV/cm in CNCBT3 to 135 kV/cm in CNCBT5, 120 kV/cm in CNCBT8, and 114 kV/cm in CNCBT12, which can be explained by the reduced domain size with higher domain wall mobility. Besides that, both the P_r and P_m increase on doping at RT (P_m = 9.8 μC/cm^2 and P_r = 6.50 μC/cm^2) for the CNCBT12 sample, which can be explained by the improved domain wall density and mobility, as reported in other ferroelectric ceramics [50,51]. Hence, it can be concluded that the introduction of Na^+ and $Ce^{3+/4+}$ ions into CBT is a viable method for the preparation of high-performance ferroelectric/piezoelectric materials for high-temperature applications.

Figures 7(a) and 7(b) show the frequency dependence of ε' and tanδ for the unpoled and poled CNCBT ceramics, respectively. Upon doping, the permittivity increases due to the reduced oxygen vacancies and improved domain wall concentration and mobility. The permittivity of all the ceramic samples decreases slightly after DC poling, which can be explained by the reduced density of non-180° domain walls and preferred domain growth [43,52]. The resonant peaks at high frequencies can be attributed to the piezoelectric effect. In addition, Table 1 summarizes the d_{33}, K_p, K_t, and Q_m for the poled CNCBT ceramics, as determined by the resonance–antiresonance method. The d_{33} increases from 5.5 pC/N (CBT) to 20.5 pC/N (CNCBT12), which can be linked with multi-sized domain structures. The normalized thermal depoling ($d_{33}(T)/d_{33}$(RT)) data for all CNCBT ceramics from RT to 700 ℃ are shown in Fig. S4 in the ESM. All values of $d_{33}(T)/d_{33}$(RT) are over 0.9 when the annealing temperature is below or around 500 ℃, suggesting good thermal stability of CNCBT12 piezoelectric ceramics. Similarly, K_t and K_p increase with the increasing content of Na and Ce, whereas Q_m shows the opposite trend. A high K_p value is usually related to higher d_{33}, which can be attributed to a high domain wall density. While the reduction of Q_m can be explained by the enhanced domain wall mobility accompanied by higher internal friction [53].

To further explore the relationship between the multiple-sized domain structure and ferroelectric/piezoelectric properties of CNCBT ceramics, the schematic diagrams are depicted in Figs. 8(a)–8(c). For a grain with various domains, as shown in Fig. 8(a), the double-well potential energy is deep, and the

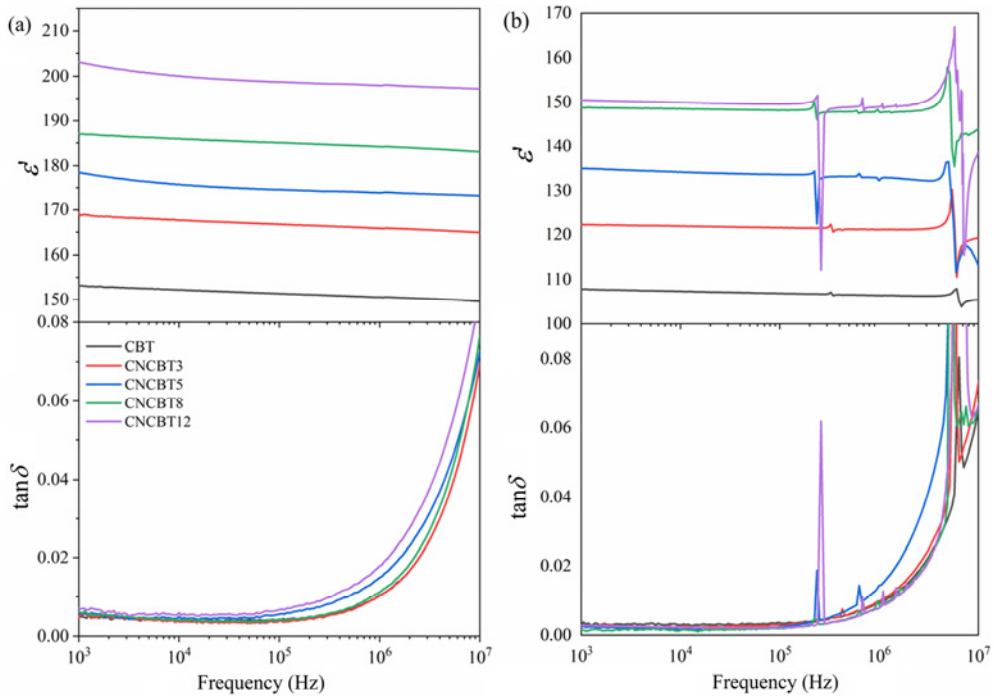

Fig. 7 ε' and tanδ as a function of frequency for (a) unpoled and (b) poled $Ca_{1-x}(Na_{0.5}Ce_{0.5})_xBi_4Ti_4O_{15}$ ceramics (x = 0, 0.03, 0.05, 0.08, and 0.12).

Table 1 K_p, K_t, Q_m, and d_{33} for CNCBT ceramics, as obtained by the resonance–antiresonance method

Composition	K_p (%)	K_t (%)	Q_m	d_{33} (pC/N)
CBT	3.3	12.5	4236	5.5±0.1
CNCBT3	4.4	16.3	3290	10.5±0.1
CNCBT5	5.3	17.8	2629	12.0±0.1
CNCBT8	6.2	18.6	2298	15.3±0.1
CNCBT12	7.3	19.7	700	20.5±0.1

saturated *P*–*E* loop is broad with the two corresponding current peaks far away from $E = 0$. When the domains become smaller, as shown in Fig. 8(b), the double-well potential energy becomes flat accompanied by a reduced distance between two minimum points of $-P_s$ and $+P_s$ (negative and positive spontaneous polarization where the Landau energy is the lowest) indicated by the red dashed lines. A slimmer *P*–*E* loop with higher P_r and two current peaks with lower E_c (indicated by the blue arrows) can be observed. The relationship between d_{33} and electrostrictive coefficient (Q) and dielectric and ferroelectric properties can be expressed by the equation of $d_{33} = 2Q\varepsilon_0\varepsilon' P_r$ (where ε_0 is the permittivity of vacuum) [54], as shown in Fig. 8(c). For perovskite ferroelectrics, the product of Q and C is constant around $(3.1 \pm 0.5) \times 10^3$ $(m^4 \cdot K)/C^2$ based on the thermodynamic analysis [55]. In this case, Q is proportional to C^{-1} for Aurivillius materials and decreases with x based on Fig. 4(f). Using a simple atomic model proposed by Newnham *et al*. [56,57], to the first approximation, the relationship between Q and dielectric properties can be written as $Q \approx 1/\varepsilon$, where

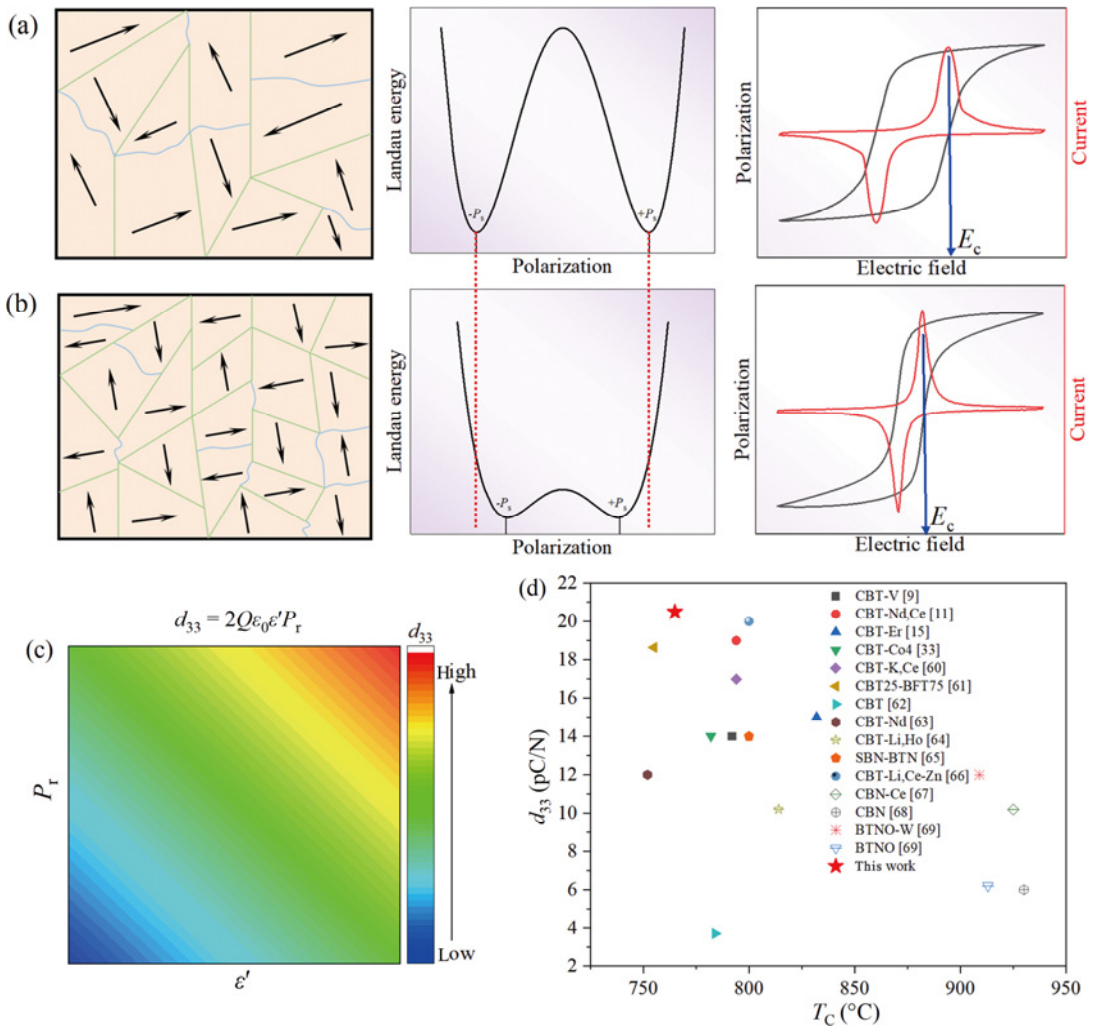

Fig. 8 Schematic diagrams of domain structures, potential energies, and hysteresis loops for (a) large-sized domains and (b) small-sized domains, where the blue curves indicate the 180° domain walls, and the green lines represent the non-180° domain walls. (c) Mapping of d_{33} at different values of P_m and ε'. (d) Comparison between d_{33} and T_C values for $x = 0.12$ sample and other Aurivillius piezoceramics reported in Refs. [9,11,15,33,60–69]. Note: BFT represents $Bi_5FeTi_3O_{15}$, SBN–BTN represents $SrBi_2Nb_2O_9$–Bi_3TiNbO_9, and BTNO represents Bi_3TiNbO_9.

ε is complex permittivity. Lower Q is related to higher dielectric permittivity, which suggest that an improved d_{33} is related to the increase of permittivity with higher x (Fig. 7). It is also reasonable that d_{33} is proportional to P_r here, which can be improved by the multi-sized domain configurations with a small backing field. A similar behaviour has been reported for other chemically modified Aurivillius materials [58]. Aside from these factors, reduced point defects like oxygen vacancies together with lower conductivity may destabilize domain structures, and then improve the domain wall mobility, thereby enhancing the piezoelectricity for CNCBT ceramics, as reported in other perovskite structured piezoelectric ceramics [59]. Overall, the enhanced d_{33} and a relatively high T_C for x = 0.12 ceramics, as compared with those for other reported Aurivillius phase ceramics in Refs. [9,11,15, 33,60–69] (Fig. 8(d)), make the Na and Ce co-doped CBT ceramics promising materials for high-temperature piezoelectric applications.

4 Conclusions

In summary, the effect of Na and Ce co-doping on the crystal structure, domain structure, and dielectric, ferroelectric, and piezoelectric properties of the Aurivillius-phase CBT-derived ceramics is investigated to prepare a high-performance piezoelectric material for high-temperature applications. The results of the XRD patterns on the $Ca_{1-x}(Na_{0.5}Ce_{0.5})_xBi_4Ti_4O_{15}$ (x = 0, 0.03, 0.05, 0.08, and 0.12) ceramics indicate that the crystal structure does not change substantially on doping, and all samples are single-phase materials with an orthorhombic structure (space group: $A2_1am$), typical of the standard four-layer-structured BLSFs. The substitution-induced increase of t was found to result in the lowering ferroelectric-to-paraelectric phase transition temperature. The enhanced dielectric behaviour of the doped samples is attributed to the reduction of oxygen vacancies by the Na and Ce co-doping. By the PFM, the multi-sized (micron and sub-micron sized) ferroelectric domain structure was observed in the doped samples. It is demonstrated that the domain size progressively decreases with the increasing concentration of Na and Ce ions. The smaller domains with higher domain wall density and mobility are suggested to be responsible for the increased polarization, reduced E_c, and enhanced piezoelectric properties of the CNCBT ceramics. The x = 0.12 ceramic sample exhibiting a high T_C (~765 ℃), large P_m (9.8 μC/cm^2), and high d_{33} (20.5 pC/N) appears to be a promising candidate for high-temperature piezoelectric applications.

Acknowledgements

This work was supported by the National Key R&D Program of China (Grant No. 2022YFB3807404) and the National Natural Science Foundation of China (Grant No. U19A2087). Zimeng Hu would like to acknowledge the China Scholarship Council (Grant No. 201806370199) for supporting this work. Vladimir Koval acknowledges the support of the Grant Agency of the Slovak Academy of Sciences (Grant No. 2/0034/23).

Declaration of competing interest

The authors have no competing interests to declare that are relevant to the content of this article. The author Haixue Yan is the Editorial Committee member of this journal.

Electronic Supplementary Material

Supplementary material is available in the online version of this article at https://doi.org/10.26599/JAC.2023.9220754.

References

[1] Yan HX, Li CG, Zhou JG, *et al*. New high T_C piezoelectric ceramics with bismuth layer structure. *Ferroelectrics* 2001, **252**: 217–223.

[2] Long CB, Wang B, Ren W, *et al*. Significantly enhanced electrical properties in $CaBi_2Nb_2O_9$-based high-temperature piezoelectric ceramics. *Appl Phys Lett* 2020, **117**: 032902.

[3] Peláiz-Barranco A, González-Abreu Y. Ferroelectric ceramic materials of the Aurivillius family. *J Adv Dielectr* 2013, **3**: 1330003.

[4] Zhang HJ, Ke H, Luo HJD, *et al*. Effects of spark plasma sintering on ferroelectricity of $0.8Bi_{3.15}Nd_{0.85}Ti_3O_{12}$–$0.2CoFe_2O_4$ composite ceramic. *J Eur Ceram Soc* 2018, **38**: 2353–2359.

[5] Maria JP, Kang XY, Floyd RD, *et al*. Cold sintering: Current status and prospects. *J Mater Res* 2017, **32**: 3205–3218.

[6] Li LL, Yuan HB, Huang PM, *et al*. Enhanced piezoelectricity and excellent thermal stabilities in Nb–Mg co-doped $CaBi_4Ti_4O_{15}$ Aurivillius high Curie temperature ceramics. *Ceram Int* 2020, **46**: 2178–2184.

[7] Liu Y, Zhang YH, Zhu LL, *et al*. Enhanced piezoelectric activity with good thermal stability and improved electrical resistivity in Ta–Mn co-doped $CaBi_4Ti_4O_{15}$ high-temperature piezoceramics. *Ceram Int* 2020, **46**: 22532–22538.

[8] Zulhadjri, Wendari TP, Ramadhani R, *et al*. La^{3+} substitution induced structural transformation in $CaBi_4Ti_4O_{15}$ Aurivillius phases: Synthesis, morphology, dielectric and optical properties. *Ceram Int* 2021, **47**: 23549–23557.

[9] Zeng JT, Li YX, Yang QB, *et al*. Ferroelectric and piezoelectric properties of vanadium-doped $CaBi_4Ti_4O_{15}$ ceramics. *Mater Sci Eng B* 2005, **117**: 241–245.

[10] Suárez DY, Reaney IM, Lee WE. Relation between tolerance factor and T_C in Aurivillius compounds. *J Mater Res* 2001, **16**: 3139–3149.

[11] Sheng LS, Du X, Chao QY, *et al*. Enhanced electrical properties in Nd and Ce co-doped $CaBi_4Ti_4O_{15}$ high temperature piezoceramics. *Ceram Int* 2018, **44**: 18316–18321.

[12] Yan HX, Zhang Z, Zhu WM, *et al*. The effect of (Li,Ce) and (K,Ce) doping in Aurivillius phase material $CaBi_4Ti_4O_{15}$. *Mater Res Bull* 2004, **39**: 1237–1246.

[13] Xin DQ, Chen Q, Wu JG, *et al*. Crystal structure, piezoelectric and dielectric properties of $(Li,Ce)^{4+}$, Nb^{5+} and Mn^{2+} co-doped $CaBi_4Ti_4O_{15}$ high-temperature ceramics. *J Electron Mater* 2016, **45**: 3597–3602.

[14] Xiao P, Zheng QJ, Tian MJ, *et al*. Enhanced ferroelectricity/piezoelectricity, bright blue/yellow emission and excellent thermal stability in $Ca_{1-x}(LiDy)_{x/2}Bi_4Ti_4O_{15}$ lead-free multifunctional ceramics. *RSC Adv* 2016, **6**: 16387–16394.

[15] Peng DF, Wang XS, Xu CN, *et al*. Bright upconversion emission, increased T_C, enhanced ferroelectric and piezoelectric properties in Er-doped $CaBi_4Ti_4O_{15}$ multifunctional ferroelectric oxides. *J Am Ceram Soc* 2013, **96**: 184–190.

[16] Larson AC, von Dreele RB. Program GSAS, General Structure Analysis System (Los Alamos National Laboratory Report No. LA-UR-86-784, Los Alamos), 1987. Available at http://public.lanl. gov/gsas.

[17] Toby BH. EXPGUI, a graphical user interface for GSAS. *J Appl Cryst* 2001, **34**: 210–213.

[18] Li XD, Chen ZN, Sheng LS, *et al*. Remarkable piezoelectric activity and high electrical resistivity in Cu/Nb co-doped $Bi_4Ti_3O_{12}$ high temperature piezoelectric ceramics. *J Eur Ceram Soc* 2019, **39**: 2050–2057.

[19] Xu Q, Xie SX, Wang F, *et al*. Bismuth titanate based piezoceramics: Structural evolutions and electrical behaviors at different sintering temperatures. *J Alloys Compd* 2021, **882**: 160637.

[20] Jain V, Biesinger MC, Linford MR. The Gaussian–Lorentzian Sum, Product, and Convolution (Voigt) functions in the context of peak fitting X-ray photoelectron spectroscopy (XPS) narrow scans. *Appl Surf Sci* 2018, **447**: 548–553.

[21] Viola G, Saunders T, Wei X, *et al*. Contribution of piezoelectric effect, electrostriction and ferroelectric/ferroelastic switching to strain–electric field response of dielectrics. *J Adv Dielectr* 2013, **3**: 1350007.

[22] Uchino K, Zheng JH, Joshi A, *et al*. High power characterization of piezoelectric materials. *J Electroceramics* 1998, **2**: 33–40.

[23] Giurgiutiu V, Zagrai AN. Characterization of piezoelectric wafer active sensors. *J Intel Mat Syst Str* 2002, **11**: 959–975.

[24] Glazer AM. Simple ways of determining perovskite structures. *Acta Cryst Sect A* 1975, **31**: 756–762.

[25] Li HY, Zhou Y, Liang ZH, *et al*. High-entropy oxides: Advanced research on electrical properties. *Coatings* 2021, **11**: 628.

[26] Yu CY, Zeng Y, Yang B, *et al*. $SrFe_{12}O_{19}$ based ceramics with ultra-low dielectric loss in the millimetre-wave band. *Appl Phys Lett* 2018, **112**: 143501.

[27] Park SJ, Lee JP, Jang JS, *et al*. *In situ* control of oxygen vacancies in TiO_2 by atomic layer deposition for resistive switching devices. *Nanotechnology* 2013, **24**: 295202.

[28] Hu ZM, Koval V, Yue YJ, *et al*. Structural evolution and coexistence of ferroelectricity and antiferromagnetism in Fe, Nb co-doped $BaTiO_3$ ceramics. *J Eur Ceram Soc* 2023, **43**: 2460–2468.

[29] Hu ZM, Zhang HF, Zhu ZG, *et al*. Deciphering the peculiar hysteresis loops of $0.05Pb(Mn_{1/3}Sb_{2/3})O_3$–$0.95Pb(Zr_{0.52}Ti_{0.48})O_3$ piezoelectric ceramics. *Acta Mater* 2023, **244**: 118563.

[30] Bharti B, Kumar S, Lee HN, *et al*. Formation of oxygen vacancies and Ti^{3+} state in TiO_2 thin film and enhanced optical properties by air plasma treatment. *Sci Rep* 2016, **6**: 32355.

[31] Chen J, Shen SH, Wu P, *et al*. Nitrogen-doped CeO_x nanoparticles modified graphitic carbon nitride for enhanced photocatalytic hydrogen production. *Green Chem* 2015, **17**: 509–517.

[32] Xi JW, Chen H, Tan Z, *et al*. Origin of high piezoelectricity in CBT-based Aurivillius ferroelectrics: Glide of $(Bi_2O_2)^{2+}$ blocks and suppressed internal bias field. *Acta Mater* 2022, **237**: 118146.

[33] Zhao TL, Wang CM, Wang CL, *et al*. Enhanced piezoelectric properties and excellent thermal stabilities of cobalt-modified Aurivillius-type calcium bismuth titanate ($CaBi_4Ti_4O_{15}$). *Mater Sci Eng B* 2015, **201**: 51–56.

[34] Shukla A, Kumar N, Behera C, *et al*. Structural, dielectric and magnetic characteristics of $Bi(Ni_{0.25}Ti_{0.25}Fe_{0.50})O_3$ ceramics. *J Mater Sci Mater Electron* 2016, **27**: 1209–1216.

[35] Lines ME, Glass AM. *Principles and Applications of Ferroelectrics and Related Materials*. Oxford, UK: Oxford University Press, 2001.

[36] Yan TX, Chen KY, Li CQ, *et al*. Structure evolution, dielectric, and conductivity behavior of $(K_{0.5}Na_{0.5})NbO_3$–$Bi(Zn_{2/3}Nb_{1/3})O_3$ ceramics. *J Adv Ceram* 2021, **10**: 809–819.

[37] Barsoum M. *Fundamentals of Ceramics*, 2nd edn. Boca Raton, USA: CRC Press, 2019.

[38] Yan HX, Zhang HT, Zhang Z, *et al*. B-site donor and acceptor doped Aurivillius phase Bi_3NbTiO_9 ceramics. *J Eur Ceram Soc* 2006, **26**: 2785–2792.

[39] Xie SX, Chen Y, Liu WY, *et al*. Three-dimensional domain patterns in tetragonal-to-monoclinic $Bi_4Ti_3O_{12}$ ceramics: Nonlinear analysis and piezoresponse force microscopy imaging. *Acta Mater* 2020, **188**: 228–240.

[40] Keeney L, Kulkarni S, Deepak N, *et al*. Room temperature

ferroelectric and magnetic investigations and detailed phase analysis of Aurivillius phase $Bi_5Ti_3Fe_{0.7}Co_{0.3}O_{15}$ thin films. *J Appl Phys* 2012, **112**: 052010.

[41] Katayama S, Noguchi Y, Miyayama M. 3D domain structure in $Bi_4Ti_3O_{12}$ crystals observed by using piezoresponse force microscopy. *Adv Mater* 2007, **19**: 2552–2555.

[42] He X, Chen C, Zeng HR, *et al*. Bismuth layer-structured ferroelectrics with non-sheet-like polyhedral microstructures. *J Am Ceram Soc* 2021, **104**: 4041–4048.

[43] Tan YQ, Viola G, Koval V, *et al*. On the origin of grain size effects in $Ba(Ti_{0.96}Sn_{0.04})O_3$ perovskite ceramics. *J Eur Ceram Soc* 2019, **39**: 2064–2075.

[44] Zhao Z, Buscaglia V, Viviani M, *et al*. Grain-size effects on the ferroelectric behavior of dense nanocrystalline $BaTiO_3$ ceramics. *Phys Rev B* 2004, **70**: 024107.

[45] Arlt G, Hennings D, de With G. Dielectric properties of fine-grained barium titanate ceramics. *J Appl Phys* 1985, **58**: 1619–1625.

[46] Cao WW, Randall CA. Grain size and domain size relations in bulk ceramic ferroelectric materials. *J Phys Chem Solids* 1996, **57**: 1499–1505.

[47] Lin DB, Zhang SJ, Li ZR, *et al*. Domain size engineering in tetragonal $Pb(In_{1/2}Nb_{1/2})O_3$–$Pb(Mg_{1/3}Nb_{2/3})O_3$–$PbTiO_3$ crystals. *J Appl Phys* 2011, **110**: 084110.

[48] Jin L, Li F, Zhang SJ. Decoding the fingerprint of ferroelectric loops: Comprehension of the material properties and structures. *J Am Ceram Soc* 2014, **97**: 1–27.

[49] Eriksson M, Yan HX, Nygren M, *et al*. Low temperature consolidated lead-free ferroelectric niobate ceramics with improved electrical properties. *J Mater Res* 2010, **25**: 240–247.

[50] Tan YQ, Zhang JL, Wu YQ, *et al*. Unfolding grain size effects in barium titanate ferroelectric ceramics. *Sci Rep* 2015, **5**: 9953.

[51] Tanwar A, Sreenivas K, Gupta V. Effect of orthorhombic distortion on dielectric and piezoelectric properties of $CaBi_4Ti_4O_{15}$ ceramics. *J Appl Phys* 2009, **105**: 084105.

[52] Zhang M, Xu XZ, Yue YJ, *et al*. Multi elements substituted Aurivillius phase relaxor ferroelectrics using high entropy design concept. *Mater Design* 2021, **200**: 109447.

[53] Damjanovic D. Ferroelectric, dielectric and piezoelectric properties of ferroelectric thin films and ceramics. *Rep Prog Phys* 1998, **61**: 1267–1324.

[54] Li F, Lin DB, Chen ZB, *et al*. Ultrahigh piezoelectricity in ferroelectric ceramics by design. *Nat Mater* 2018, **17**: 349–354.

[55] Li F, Jin L, Xu Z, *et al*. Electrostrictive effect in ferroelectrics: An alternative approach to improve piezoelectricity. *Appl Phys Rev* 2014, **1**: 011103.

[56] Newnham RE. *Properties of Materials: Anisotropy, Symmetry, Structure*. Oxford, UK: Oxford University Press, 2005.

[57] Newnham RE, Sundar V, Yimnirun R, *et al*. Electrostriction: Nonlinear electromechanical coupling in solid dielectrics. *J Phys Chem B* 1997, **101**: 10141–10150.

[58] Xie XC, Zhou ZY, Wang TZ, *et al*. High temperature impedance properties and conduction mechanism of W^{6+}-doped $CaBi_4Ti_4O_{15}$ Aurivillius piezoceramics. *J Appl Phys* 2018, **124**: 204101.

[59] Ren X. Large electric-field-induced strain in ferroelectric crystals by point-defect-mediated reversible domain switching. *Nat Mater* 2004, **3**: 91–94.

[60] Yan HX, Li CG, Zhou JG, *et al*. A-site (MCe) substitution effects on the structures and properties of $CaBi_4Ti_4O_{15}$ ceramics. *Jpn J Appl Phys* 2000, **39**: 6339–6342.

[61] Moure C, Lascano L, Tartaj J, *et al*. Electrical behaviour of $Bi_5FeTi_3O_{15}$ and its solid solutions with $CaBi_4Ti_4O_{15}$. *Ceram Int* 2003, **29**: 91–97.

[62] Yan HX, Li CG, Zhou JG, *et al*. Effects of A-site (NaCe) substitution with Na-deficiency on structures and properties of $CaBi_4Ti_4O_{15}$-based high-Curie-temperature ceramics. *Jpn J Appl Phys* 2001, **40**: 6501–6505.

[63] Zeng JT, Li YX, Wang D, *et al*. Electrical properties of neodymium doped $CaBi_4Ti_4O_{15}$ ceramics. *Solid State Commun* 2005, **133**: 553–557.

[64] Xiao P, Guo YQ, Tian MJ, *et al*. Improved ferroelectric/piezoelectric properties and bright green/UC red emission in (Li,Ho)-doped $CaBi_4Ti_4O_{15}$ multifunctional ceramics with excellent temperature stability and superior water-resistance performance. *Dalton Trans* 2015, **44**: 17366–17380.

[65] Jiménez B, Castro A, Pardo L, *et al*. Electric and ferro-piezoelectric properties of $(SBN)_{1-x}(BTN)_x$ ceramics obtained from amorphous precursors. *J Phys Chem Solids* 2001, **62**: 951–958.

[66] Xi JW, Xing J, Yuan J, *et al*. Preparation and characterization of Zn-modified $CaBi_4Ti_4O_{15}$ piezoelectric ceramics with lower sintering temperature. *J Mater Sci Mater Electron* 2020, **31**: 8805–8814.

[67] Tian XX, Qu SB, Pei ZB, *et al*. Microstructure, dielectric, and piezoelectric properties of Ce-modified $CaBi_2Nb_2O_9$ ceramics. *Ferroelectrics* 2010, **404**: 127–133.

[68] Chen HB, Shen B, Xu JB, *et al*. Correlation between grain sizes and electrical properties of $CaBi_2Nb_2O_9$ piezoelectric ceramics. *J Am Ceram Soc* 2012, **95**: 3514–3518.

[69] Zhou ZY, Dong XL, Chen H, *et al*. Structural and electrical properties of W^{6+}-doped Bi_3TiNbO_9 high-temperature piezoceramics. *J Am Ceram Soc* 2006, **89**: 1756–1760.